Journal of Materials Science: Materials in Electronics (2018) 29:9258–9267
https://doi.org/10.1007/s10854-018-8955-x

3D nanocomposite archiecture constructed by reduced graphene oxide, thermally-treated protein and mesoporous $NaTi_2(PO_4)_3$ nanocrystals as free-standing electrodes for advanced sodium ion battery

Liang Xu[1] · Guobao Xu[1] · Zhuo Chen[1] · Xiaolin Wei[1] · Juexian Cao[1] · Liwen Yang[1]

Received: 8 January 2018 / Accepted: 16 March 2018 / Published online: 23 March 2018

Abstract

$NaTi_2(PO_4)_3$ (NTP) with NASICON structure has been regarded as a promising material for sodium-ion batteries (SIBs). However, NTP always exhibits poor cycling stability and rate performance due to slow electronic conductivity. In this work, a free-standing 3D nanocomposite constructed by reduced graphene oxide (rGO), thermally-treated protein (TP) and mesoporous $NaTi_2(PO_4)_3$ nanocrystals (denoted as MNTP-TP@rGO) is reported. The fabrication includes an electrostatic self-assembly, freeze-drying, mechanical pressing and thermal treatment. In the MNTP-TP@rGO nanocomposite, 3D interconnected carbon network of rGO and TP acts as both a support for the anchored well-distributed MNTP nanocrystals and a current collector. When free-standing MNTP-TP@rGO is used directly as anode in coin-type half-cell, it delivers a high-rate capacity (52.8 $mAhg^{-1}$ at 50C) and robust cycling stability with the capacity retention of 80% after 1000 cycles at 5C. Furthermore, a full Na-ion battery is constructed using $Na_3V_2(PO_4)_3$/C (NVP/C) as a cathode and free-standing MNTP-TP@rGO as an anode and it exhibits a high specific capacity (58 $mAhg^{-1}$ at 1C) and outstanding cycling stability (98% capacity retention over 100 cycles at 1C). Our results suggest great potential of the free-standing electrode of MNTP-TP@rGO composite in high-performance SIBs.

1 Introduction

Lithium-ion batteries (LIBs) are serving as power sources in the electronic device market such as smartphone, portable computer [1–4], due to high energy density and long cycling stability [5–7]. However, with the increasing need for energy storage systems, the limited lithium source can hardly meet the requirements of commercial application [8]. Thus, it is highly important to seek for new energy system to replace LIBs. As a result, sodium-ion batteries have attracted intensive attention because of abundant resources, easy accessibility and low cost. Nevertheless, the development of SIBs is hampered by the deficiency of anode materials with rapid Na^+ insertion and extraction due to larger ionic radius and molar mass of Na compared to Li [9, 10]. Despite recent efforts are developing new anode materials such as TiO_2 [11], $Li_4Ti_5O_{12}$ [12], MoS_2 [13] and hard carbon [14–16], it is still challenging to develop suitable anode material with high-rate capability, long-term cycle life and excellent safety.

Recently, $NaTi_2(PO_4)_3$ (NTP) with Na ion super ionic conductor (NASICON) structure allowing for rapid Na^+ diffusion in the lattice [17, 18], has been considered as a promising anode material for SIBs [19, 20]. Unfortunately, pure NTP exhibits poor electrochemical performance due to low electric conductivity, thereby making its practical application difficult [21]. To conquer the intrinsic shortcoming, carbonaceous material like graphene [22], carbon nanotube [12] and mesoporous carbon have been often used as a conductive medium for NTP in SIBs. These methods aforementioned can not only shorten transport paths for both electrons and Na ions, but also relieve the strain due to Na ions insertion and extraction in active materials [23]. For instance, Wu's group reported a NTP/graphene composite with superior high-rate capability of 67 $mAhg^{-1}$ at 50C. Fang's group prepared a composite of graphene decorated NTP microsphere with ultrahigh rate capability (38 $mAhg^{-1}$

✉ Liwen Yang
ylwxtu@xtu.edu.cn

[1] Hunan Key Laboratory of Micro-Nano Energy Materials and Devices, School of Physics and Optoelectronics, Xiangtan University, Hunan 411105, China

at 200C) and long-term cyclability of 77% capacity retention after 1000 cycles at 20C [22]. Although the combinations of NTP with different carbonaceous materials have made great contributions to improving electrochemical performance of NTP [24–27], most of them still require the use of insulating polymeric binder, conductive additive, and metallic current collector during electrode assembling. The addition of insulating binder is harmful to electronic kinetics and cycling stability due to the blockage of ion diffusion channels. In particular, the conductive additive and current collector adversely affect the electrode performance including energy and power densities. Thus, it is highly desirable to build free-standing NTP/carbon composite to spur its application in high-performance SIBs.

In this work, we fabricated a free-standing 3D nanocomposite constructed by reduced graphene oxide, thermally-treated protein and mesoporous NTP nanoparticles via an electrostatic self-assembly, freeze-drying, mechanical pressing and thermal treatment. In such nanocomposite, free-standing 3D interconnected carbon network of rGO and TP not only act as both binder and current collector which has an enormous decrease in the cost and weight of electrode, but also, provide 3D conduction pathway enabling rapid charge transfer. In addition, the 3D carbon network is an ideal buffer to accommodate the volume change of the anchored well-distributed MNTP nanocrystals during Na ion insertion/extraction, thereby improving electrode stability. When free-standing MNTP-TP@rGO nanocomposite is used directly as an anode in coin-type half-cell, it exhibits a high capacity of 114 $mAhg^{-1}$ at 1C, excellent rate capacity of 52 $mAhg^{-1}$ at 50C, and robust cycling stability with the capacity remains of 80% after 1000 cycles. Furthermore, a full Na-ion battery is constructed using $Na_3V_2(PO_4)_3$/C (NVP/C) as a cathode and free-standing MNTP-TP@rGO as a anode is fabricated and high initial capacity of 58 $mAhg^{-1}$ at 1C and 98% capacity retention over 100 cycles at 1C is demonstrated.

2 Experimental section

2.1 Preparation of free-standing MNTP@rGO nanocomposite

Free-standing MNTP-TP@rGO nanocomposite was prepared by an electrostatic self-assembly, freeze-drying, mechanical pressing and thermal treatment process. In a typical experiment, MNTP (100 mg) synthesized by the method in our previous report [28] ,was firstly added into 50 ml deionized water containing about 50 mg of bovine serum albumin (BSA, Aladdin Industrial Corporation) and was sonicated for 10 min using ultrasonic cell smash to make MNTP nanocrystals decorated with BSA. Then, 3.95 g NH_4HCO_3 were added into the solution including BSA decorated MNTP nanoscystals under stirring for 10 min at room temperature. Thirdly, the mixed solution was dropwise added into 50 ml GO aqueous solution with concentration about 2 mg/ml under stirring to produce flocculent gel of BSA decorated MNTP nanoscrytals and GO. Fourthly, producing flocculent gel was collected by freeze-drying procedure. Finally, the 3D aerogel was mechanically pressed into thin planchets and then were thermally treated at 350 °C for 2 h to obtain free-standing MNTP-TP@rGO composite.

2.2 Materials characterization

The crystal structure of all samples was characterized by X-ray diffraction (XRD, Rigaku D/max 2500). The microstructure and morphology of samples were characterized by scanning electron microscopy (SEM) and transmission electron microscopy (TEM), respectively. Raman profiles were obtained on a Renishaw inVia system with 532 nm excitation wavelength. Thermal gravimetric analysis (TGA) and differential scanning calorimetry (DSC) were measured using a TGA 2050 thermo gravimetric analyzer with heating rate of 10 °C min^{-1} from room temperature to 700 °C in air. The Fourier transform infrared (FTIR) spectra were obtained on a FTS-3000 FTIR spectrophotometer.

2.3 Electrochemical characterization

The electrochemical performances of the free-standing MNTP-TP@rGO nanocomposite were tested in the two-electrode CR2032 cells. The free-standing MNTP-TP@rGO nanocomposite was directly used as an anode without additional binders, conductive additive, and metallic current collector. For comparison, the reference electrode was fabricated by mixing the obtained MNTP nanocrystals, super P carbon black, and polyvinylidene fluoride (PVDF) binders with a weight ratio of 70:20:10 in *N*-methylpyrroldone, subsequently, coating on a Cu foil and finally dried at 120 °C for 12 h in a vacuum oven. The NVP/C electrode was prepared by mixing active materials, super P carbon black and PVDF at the mass ratio of 8:1:1 onto an Al foil. All coin cells were assembled in an argon-filled glove box using metallic sodium disc as the counter electrode and glass fiber (Whatman GF/D) as the separator. The electrolyte was 1.0 mol L^{-1} $NaClO_4$ dissolved in a solvent of ethylene carbonate (EC) and propylene carbonate (PC) with a volume ratio of 1:1. Galvanostatic charging–discharging (GCD) measures were performed at a voltage window of 1.5 ~ 3.0 V (vs. Na/Na^+) on a multi-channel battery testing system (NEWARE BTS-610). Cyclic voltammetry (CV) tests were carried out on an electrochemical workstation (CHI660E) in the voltage range of 1.5–3.0 V (vs. Na/Na^+) at different scan rates. Electrochemical impedance spectroscopy (EIS) tests were carried

out in the frequency range from 0.01 Hz to 100 kHz on a CHI660E electrochemical workstation. The sodium full cell was assembled using NVP/C as a cathode and free-standing MNTP-TP@rGO nanocomposite as anode. The preparation of NVP/C is using the method reported by the previous report [29]. The mass ratio of active materials between cathode and anode is 1.2:1.

3 Results and discussion

Schematic illustration for the fabrication of free-standing MNTP-TP@rGO nanocomposite is summarized in Fig. 1, including an electrostatic self-assembly between BSA-decorated MNTP nanocrystals and GO, freeze-drying, mechanical pressing and thermal treatment. In our experiments, the BSA was used as multi-functional agent to enhance the electrochemical and mechanical properties due to its outstanding adhesion ability to solid surfaces. Hence, the MNTP nanocrystals were firstly decorated with the BSA molecules through a simple dipping process. According to our previous studies, the BSA-decorated MNTP nanocrystals redispered in NH_4HCO_3 solution are positively charged [28]. On the other hand, GO sheets obtained via the modified Hummers method are highly negatively charged in water [12]. These suggest that as above solutions mixed, electrostatic interaction between BSA-decorated MNTP nanocrystals and GO sheets quickly occurs, accompanying the production of flocculent intermediate of BSA-decorated MNTP-TP and GO. Owing to relatively large density, this highly stable flocculent intermediate sinks spontaneously to the bottom (see Image I in Fig. 1), benefiting following collection. The collected intermediate was readily transferred into 3D consecutive dish-like aerogel (see Image II in Fig. 1) via a freeze-drying procedure. The aerogel is plastically so as to be deformed via mechanical pressing and punching, producing free-standing 3D intermediate of BSA-decorated MNTP nanocrystals and GO with diameter of 1.5 cm. After thermal annealing at 350 °C, free-standing 3D MNTP-TP@rGO nanocomposite was obtained accompanying the reduction of GO to rGO and the formation of thermally-treated BSA. As shown in Image III of Fig. 1, the resultant 3D nanocomposite has mechanical robustness (even under bending), suggesting direct use as free-standing anode for SIBs.

Figure 2a displays typical cross-section SEM images of free-standing 3D MNTP-TP@rGO nanocomposite, demonstrating the thickness of about 50 μm. High-magnification SEM images (Fig. 2b) reveal highly-dispersible MNTP nanocrystals adhere to surrounding interconnected carbon framework of rGO and thermally-treated BSA. Figure 2c, d show typical TEM images of free-standing 3D MNTP-TP@rGO nanocomposite, indicating that MNTP nanocrystals attach tightly to surrounding interconnected carbon framework of rGO and thermally-treated BSA. TGA/DSC were performed. The gradual weight loss in the TGA curve (see Fig. 3a) starting from 350 up to 500 °C mainly associates with the decomposition of thermally treated BSA, which is consistent with previous study [30]. When the temperature is higher than 500 °C, weight loss is occurred sharply because the rGO sheets are completely combusted. According to TGA/DSC results, free-standing MNTP@rGO film is roughly composed of 58 wt% MNTP nanocrystals, 36.5 wt% rGO and 5.5 wt% thermally-treated BSA.

Figure 3b shows XRD patterns of free-standing 3D MNTP-TP@rGO nanocomposite and referenced MNTP nanocrystals, revealing that main peaks are attributed to

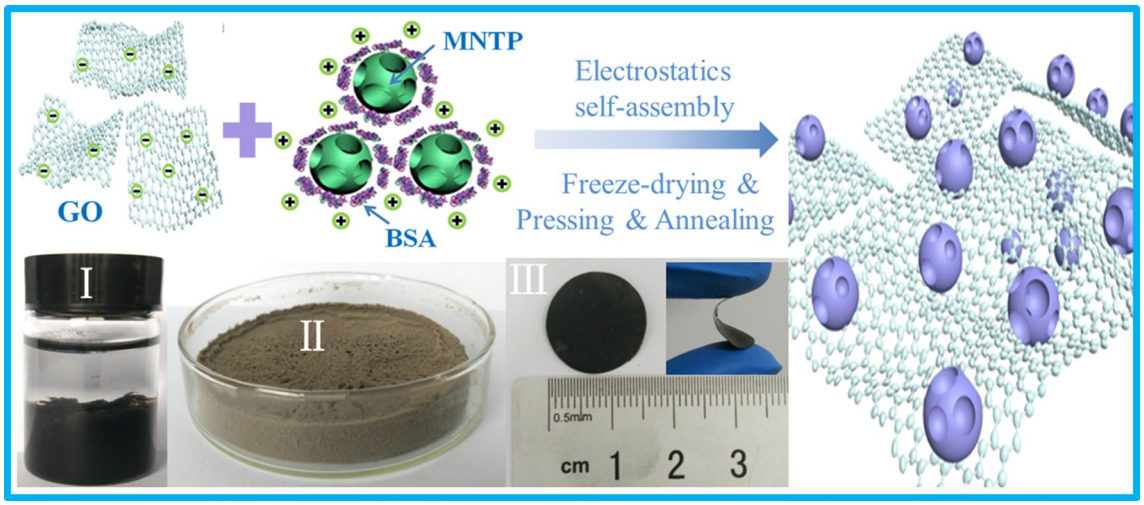

Fig. 1 Schematic illustration of the fabrication procedures and digital images of the macroscopically visible self-assembled intermediate and free-standing MNTP-TP@rGO nanocomposite

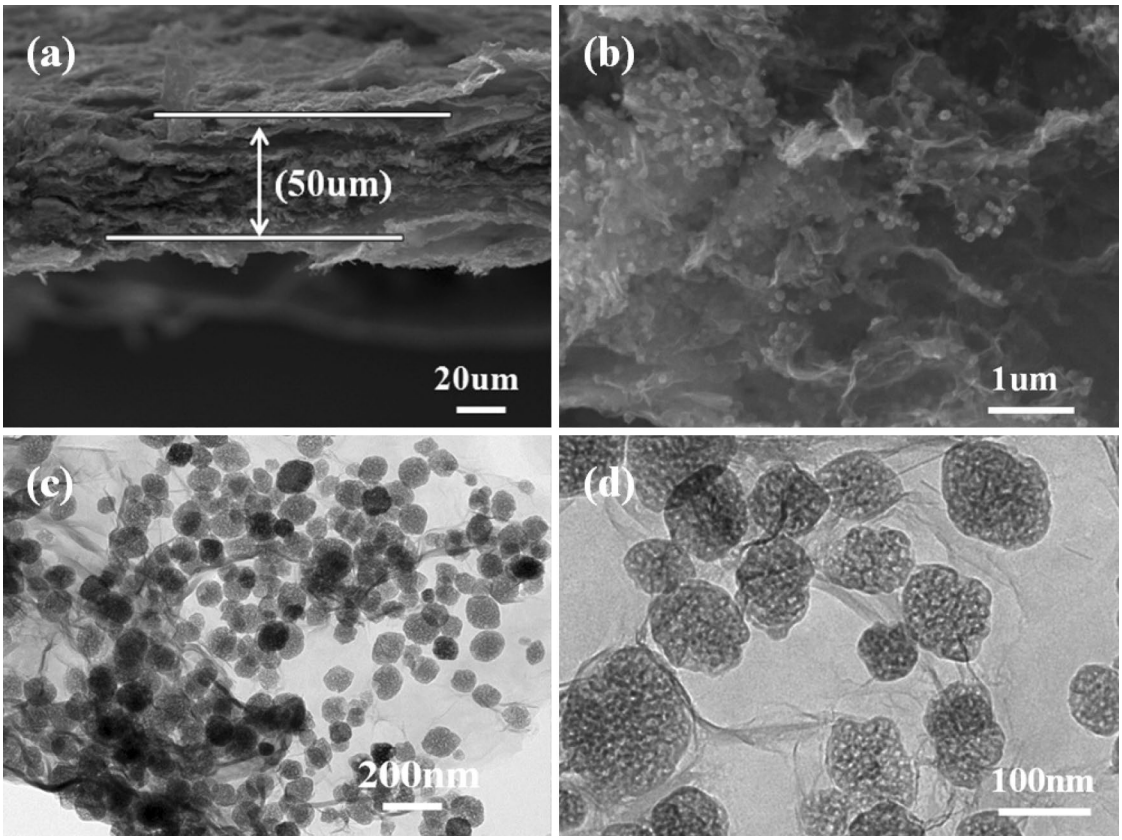

Fig. 2 **a**, **b** Typical SEM images of the free-standing MNTP-TP@rGO nanocomposite at low and high magnification, respectively; **c**, **d** typical TEM images of the free-standing MNTP-TP@rGO nanocomposite at low and high magnification, respectively

NASICON-type NTP (JCPDS no. 01-085-2265), which are also consistent with previous results about NTP [25, 31]. In addition, The XRD peak at 26.4° originates from rGO, indicating that GO has been completely reduced. Particularly, its weak and broad feature implies that self-stacking of rGO has been effectively suppressed by embedded MNTP nanocrystals. Figure 3c shows the Raman spectra of free-standing MNTP@rGO film and referenced samples. The Raman peaks at 990 and 1085 cm^{-1} are assigned to symmetrical and asymmetrical stretching in the MNTP host. The Raman bands at 155 and 272 cm^{-1} are associated with translational vibration of Ti^{4+} ions and those at 306, 341, and 438 cm^{-1} are related to PO_4^{3-} [32]. The strong Raman peaks at approximately 1350 and 1594 cm^{-1} are attributed to characteristic D from disordered carbon and G bands from sp^2 hybridized carbon, respectively. Furthermore, Fig. 3d shows FTIR profiles of free-standing 3D MNTP-TP@rGO nanocomposite and referenced samples. The broad band at 3411 cm^{-1} is characteristic of –COOH and –OH hydroxyl groups. The bands at 570 and 1032 cm^{-1} are assigned to the P–O bonds in PO_4 tetrahedra, and those at 640 and 997 cm^{-1} belong to Ti–O bonds in TiO_6 octahedra. In addition, one broad shoulder peak related to characteristic C–C stretching vibration of aromatic skeleton appears at 1573 cm^{-1} in 3D MNTP-TP@rGO nanocomposite [9, 33]. The aforementioned results confirm the co-existence of MNTP nanocrystals in 3D carbon framework of rGO and thermally-treated BSA.

The sodium storage performance of free-standing 3D MNTP-TP@rGO nanocomposite as working electrode was characterized in coin-type (CR 2032) half-cell using metallic Na foil as the counter and reference electrode. Figure 4a displays the cyclic voltammetry (CV) curves for both 3D MNTP-TP@rGO nanocomposite and referenced MNTP nanocrystals at a scan rate of 0.5 mVs^{-1} in the potential range between 1.5 and 3.0 V (vs. Na^+/Na). A pair of well-defined redox peaks corresponding to the oxidation and reduction of $Ti^{3+} \leftrightarrow Ti^{4+}$ through a Na^+ insertion-extraction reaction mechanism [$NaTi_2(PO_4)_3 + 2Na^+ + 2e^- \leftrightarrow Na_3Ti_2(PO_4)_3$] is observed in both samples [34]. However, the voltage differences between oxidation and reduction peaks, which reflecting the polarization degree of electrode, of free-standing 3D MNTP-TP@rGO nanocomposite is smaller than that of referenced MNTP nanocrystals. The results imply superior ion/electron conductivity endowed by 3D carbon framework of rGO and

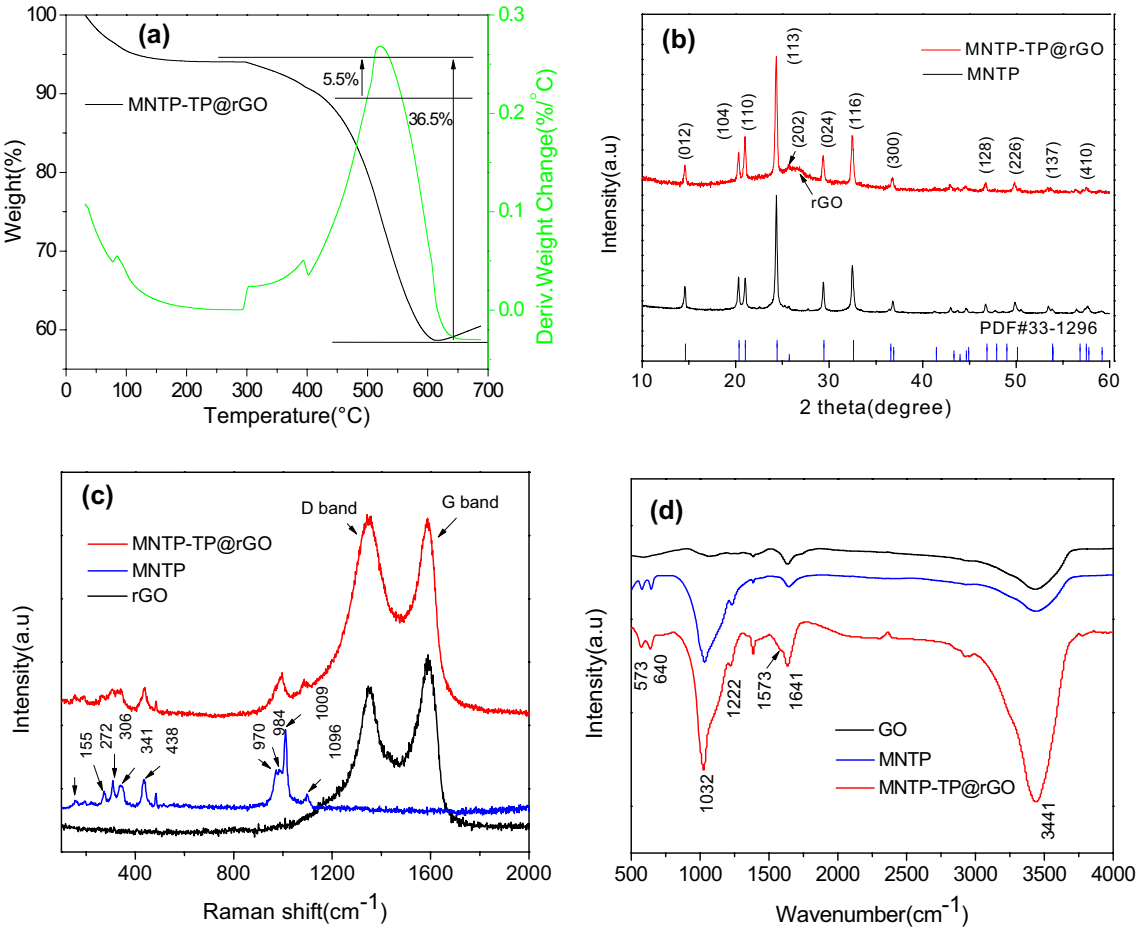

Fig. 3 **a** TGA/DSC curves of the free-standing MNTP-TP@rGO nanocomposite; **b** XRD patterns of the free-standing MNTP-TP@rGO nanocomposite and referenced MNTP nanocrytals; **c**, **d** Raman and FTIR spectra of the free-standing MNTP-TP@rGO nanocomposite and referenced samples

thermally-treated BSA, which is favorable for depressing the electrode polarization to benefit sodium storage. Figure 4b depicts the GCD profiles of free-standing 3D MNTP-TP@rGO nanocomposite at a current rate of 1C (1C = 133 mAg^{-1}) for 1st, 2nd, 100th and 200th cycles. Well-defined flat voltage plateaus with symmetrical feature at about ~ 2.1 V associated with the redox reaction of $Ti^{3+} \leftrightarrow Ti^{4+}$ are observed. The electrochemical polarizations between the charge and discharge plateau is about 100 mV for 1st cycle. The small electrochemical polarizations keep almost unchanged upon cycling, confirming high ion/electron conductivity due to unique architecture of well-distributed MNTP nanocrystals embedded in monolithic 3D carbon framework of rGO and thermally-treated BSA. The free-standing 3D MNTP-TP@rGO nanocomposite delivers initial discharging and charging capacities of 114.1 and 113.1 $mAhg^{-1}$ with a high Coulombic efficiency (CE) of 98.8%, indicating outstanding electrochemical reversibility. Figure 4c shows the GCD profiles of free-standing 3D MNTP-TP@rGO nanocomposite at various current densities from 0.5 to 50C, demonstrating similarly symmetrical shape in spite of serious polarization beyond 30C indicative of suprior rate performance. The rate performance of free-standing 3D MNTP-TP@rGO nanocomposite at various discharge C-rates is shown in Fig. 4d. Compared with relatively poor rate performance of pure MNTP, the free-standing 3D MNTP-TP@rGO nanocomposite delivers high reversible capacities of 122, 114, 106, 94, 85, 76 and 68 $mAhg^{-1}$ at current rates of 0.5, 1, 2, 5, 10, 20 and 30C, respectively. Even at a high rate of 50C, a stable reversible capacity of 52 $mAhg^{-1}$ was preserved. Moreover, when the current rate is turned back to 0.5C, a high capacity of 118 $mAhg^{-1}$ is recovered rapidly, indicating superior structural stability of electrode. Figure 4e shows the cycling performance of the free-standing 3D MNTP-TP@rGO nanocomposite at 1C, demonstrating that after 200 cycles, a reversible capacity is still kept as high as 101 $mAhg^{-1}$ with a capacity of 91.6% retention. In contrast, the pure MNTP nanocrystal exhibits serious capacity fading with capacity retention of only 49.4% after 200

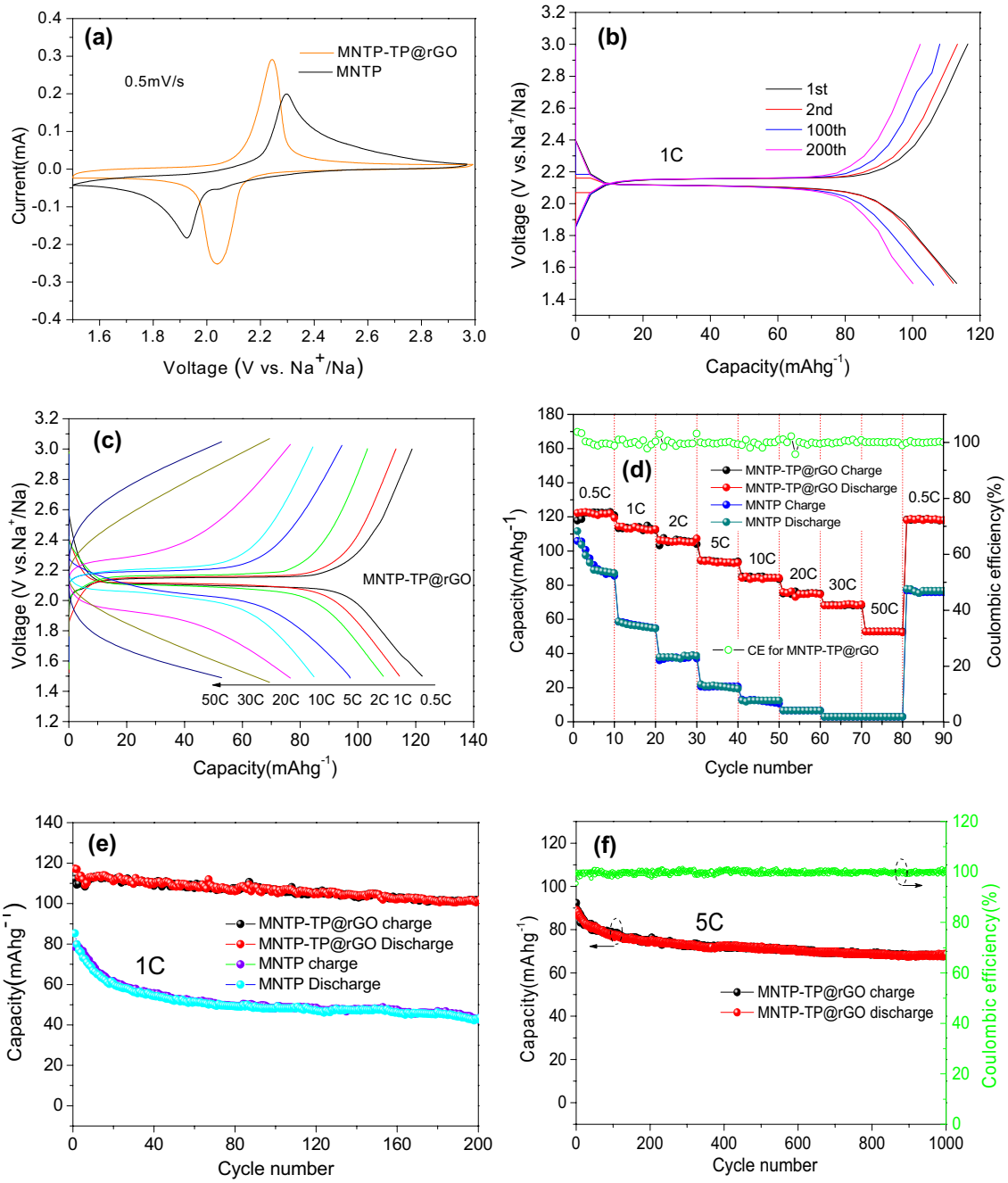

Fig. 4 **a** CV curves of the free-standing MNTP-TP@rGO nanocomposite and referenced MNTP nanocrystals at 0.5 mVs^{-1}; **b** GCD curves for the free-standing MNTP-TP@rGO nanocomposite of 1st, 2nd, 100th and 200th cycles at 1C; **c** GCD curves of the free-standing MNTP-TP@rGO nanocomposite at 0.5, 1, 2, 5, 10, 20, 30 and 50C; **d** Rate performance and Coulombic efficiency of the free-standing MNTP-TP@rGO nanocomposite and referenced NTP nanocrystals at different current densities from 0.5 to 50C; **e** Cycle performances of the free-standing MNTP-TP@rGO nanocomposite and referenced NTP nanocrystals at 1C for 200 cycles; **f** Long cycling performance and Coulombic efficiency (CE) of the the free-standing MNTP-TP@rGO nanocomposite at a high current rate of 5C for 1000 cycles

cycles. Furthermore, long cycling performance of the free-standing 3D MNTP-TP@rGO nanocomposite at a high rate of 5C is also investigated and the result is presented in Fig. 4f. The free-standing electrode exhibits outstanding cycling performance with about 77.2% retention of the initial capacity and high CE values of 99% after 1000 cycles, confirming that its superior cyclability and reversibility as an anode for high-performance SIBs.

To further explore superior reaction kinetic behavior of the free-standing 3D MNTP-TP@rGO nanocomposite

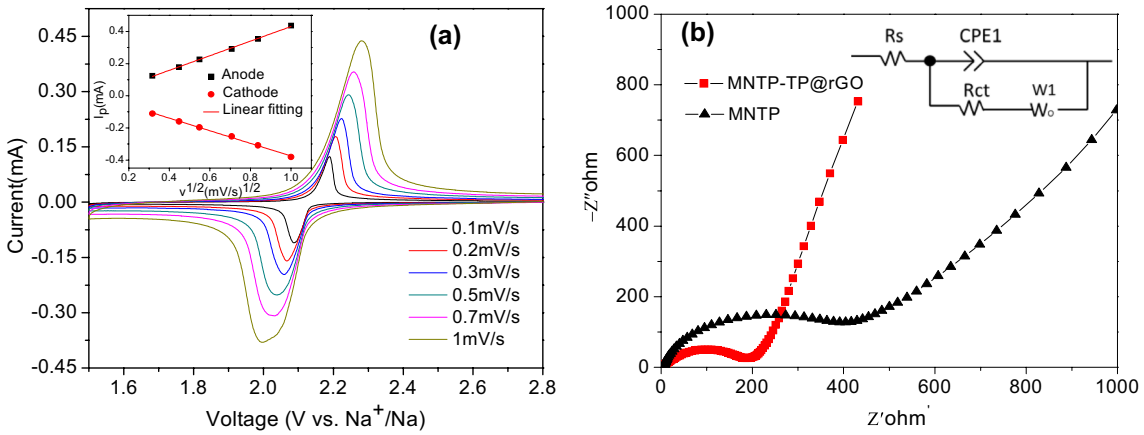

Fig. 5 **a** CV curves of the free-standing MNTP-TP@rGO nanocomposite at various scan rates and the relationship between the peak current (I_p) and the square root of scan rate ($v^{1/2}$) (the inset); **b** Nyquist plots of the free-standing MNTP-TP@rGO nanocomposite and referenced NTP nanocrystals. The inset shows the equivalent circuit model

electrode. Figure 5a shows the CV profiles of the free-standing 3D MNTP-TP@rGO nanocomposite at various sweep rates from 0.1 to 1 mVs^{-1}, which reveals that the peak current of the redox peaks increase with the bigger scan rate. Moreover, the inset presents the nicely linear relationship between the peak current (I_p) and the square root of the scan rate ($v^{1/2}$). The result confirms that the two-phase mechanism in MNTP-TP@rGO is a diffusion-controlled behavior. The "apparent diffusion coefficient" of Na^+ can be calculated based on the Randles–Sevcik equation:

$$I_p = 2.69 \times 10^5 n^{3/2} A C D^{1/2} v^{1/2} \quad (1)$$

where I_p, n, A, C, D, and v are the peak current (A), electron number per species reaction, active surface area of the electrode (cm^2), concentration of Na^+ in the electrode (mol cm^{-3}), apparent diffusion coefficient of Na^+ (cm^2 s^{-1}) and scanning rate (Vs^{-1}), respectively. The calculated apparent diffusion coefficients of the free-standing 3D MNTP-TP@rGO nanocomposite are 2.13×10^{-11} and 1.58×10^{-11} cm^2 s^{-1} for the anodic and cathodic reactions, indicating that the MNTP-TP@rGO composite exhibits excellent ability for rapid Na^+ diffusion.

In addition, the Nyquist plots of the free-standing 3D MNTP-TP@rGO nanocomposite and referenced sample were measured after the rate capacity test as shown in Fig. 5b. The result reveals a semicircle in the high-middle frequency range and straight line in low frequency region both for two samples. In general, the semicircle is associated with charge transfer resistance (R_{ct}) between the electrolyte and electrode. According to the inset equivalent circuit model, the R_{ct} value of the free-standing 3D MNTP-TP@rGO nanocomposite is 180 Ω, which is smaller than that (397 Ω) aquired from the referenced MNTP nanocrystals. The results suggest that the 3D interconnected carbon network of rGO and TP reduces polarization, resulting in efficient charge transport between the MNTP nanocrystals and electrolyte during discharging and charging, which is a factor for superior Na storage of free-standing 3D MNTP-TP@rGO nanocomposite.

The Na^+ diffusion coefficient (D_{Na}) under the state of charge is another key indicator of kinetics behavior in an electrochemical reaction, and it can be calculated based on the following equations:

$$D_{Na} = \frac{R^2 T^2}{2A^2 n^4 F^4 C^2 \sigma^2} \quad (2)$$

$$Z' = R_s + R_{ct} + \sigma \omega^{-1/2} \quad (3)$$

where T, R, A, n, F, and C are the absolute temperature, gas constant, surface area of the electrode, number of electrons transferred in the half reaction of the redox couple, Faraday's constant and Na^+ concentration, respectively. σ is the Warburg factor and its value can be obtained from the slope of the lines between Z' and $\varpi^{-1/2}$ in the low frequency region. The cell is fully charged for the EIS measurement in our test. According to the EIS measurement, the calculated D_{Na} values of the free-standing 3D MNTP-TP@rGO nanocomposite is much bigger than that from the referenced MNTP nanocrystals (see Table 1). The comparative results indicate

Table 1 Values of R_{ct}, σ and D_{Na} for MNTP and MNTP-TP@rGO electrodes in half-cells according to Fig. 5b

Samples	R_{ct} (Ω)	σ	D_{Na} (cm^2 s^{-1})
MNTP	397	567.8	6.616×10^{-15}
MNTP-TP@rGO	180	59.4	5.935×10^{-14}

that the 3D interconnected carbon network of rGO and TP enable quick migration of Na^+ into the interior of MNTP nanocrystals, thereby leading to superior rate capability and cycle performance.

To evaluate practical application of the free-standing 3D MNTP-TP@rGO nanocomposite as an anode for SIBs, an all-NASICON-type full Na-ion battery schematically illustrated in Fig. 6a was assembled, using the NVP/C composite as a cathode (denoted as MNTP-TP@rGO//NVP/C).

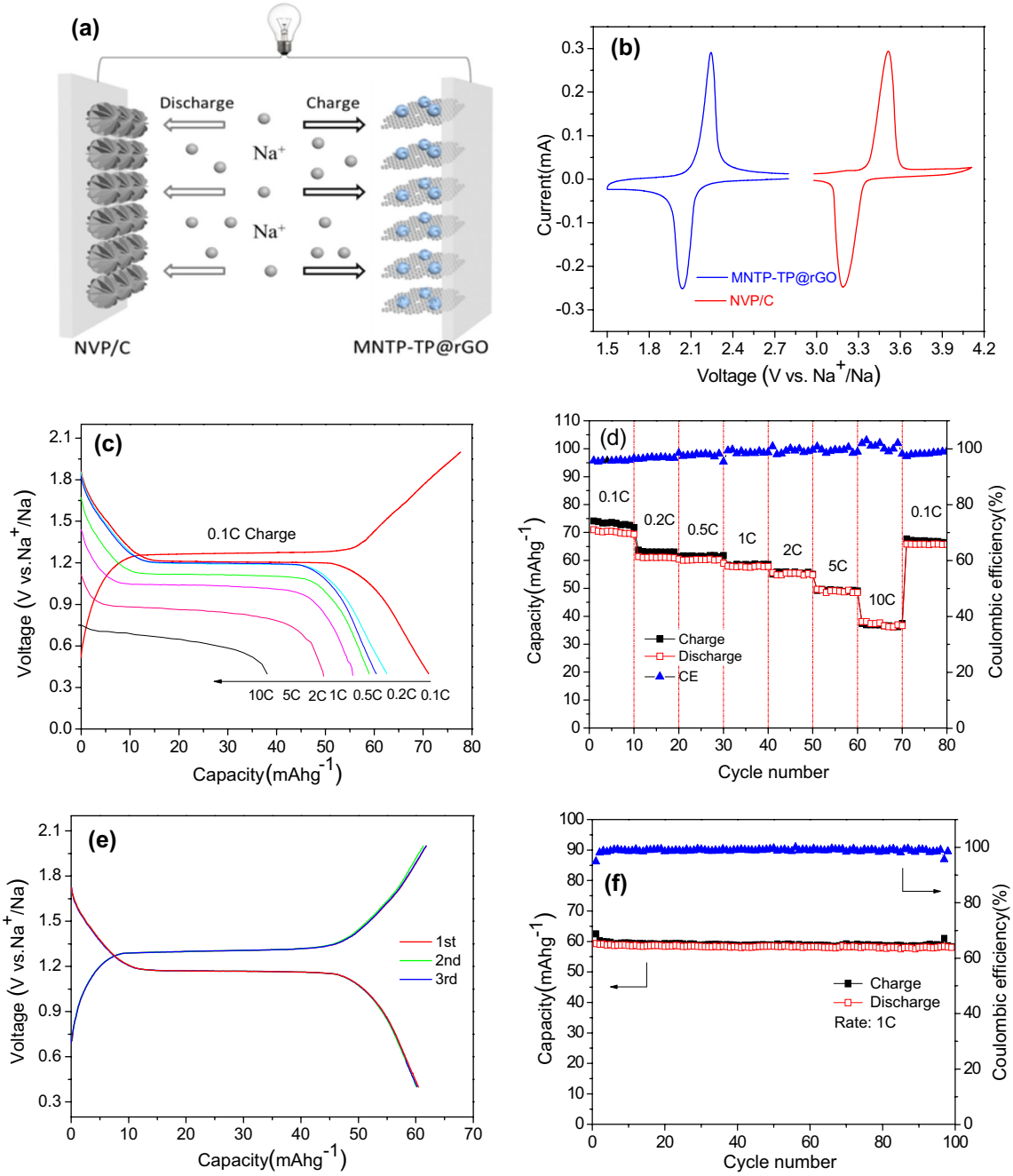

Fig. 6 **a** Schematic illustration of sodium ion full cell using NVP/C as the cathode and free-standing MNTP-TP@rGO nanocomposite as the anode; **b** CV curves of free-standing MNTP-TP@rGO nanocomposite and NVP/C electrodes at a scan rate of 0.5 mVs^{-1} during half-cell test; **c** GCD curves of the MNTP-TP@rGO//NVP/C full cell full cell at various rates; **d** Rate performances and Coulombic efficiency of the MNTP-TP@rGO//NVP/C full cell full cell with current rates range from 0.1 to 10C; **e** GCD curves for the MNTP-TP@rGO//NVP/C full cell of 1st, 2nd, and 3th cycles at 1C; **f** Cycling performance of the MNTP-TP@rGO//NVP/C full cell at a current rate of 1C

Figure 6b shows the CV curves of the free-standing 3D MNTP-TP@rGO nanocomposite and NVP/C composite. Both electrodes display a pair of well-defined redox peaks during half-cell test, which are consistent with previous reports [35]. Figure 6c, d exhibit the charge–discharge profiles and rate performance of a full cell at various current rates with the voltage range from 0.4 to 2 V, respectively. The full cell demonstrates a charge–discharge plateau of about 1.2 V and discharge capacities (based on the mass of MNTP-TP@rGO anode) of 71, 61, 60, 58, 55, 49 and 38 $mAhg^{-1}$ at 0.1, 0.2, 0.5, 1, 2, 5 and 10C (1C = 133 mAg^{-1}), respectively. When the current is turned back to 0.5C, the discharge capacity is still remained 65 $mAhg^{-1}$, indicating superior reversible and stable performance of the full cell. The cycling performance of the MNTP-TP@rGO//NVP/C full cell was also evaluated at the current rate of 1C. As shown in Fig. 6e, f, the full cell delivers an initial discharge capacity of 59 $mAhg^{-1}$ and 98% of the initial capacity is retained after 100 cycles. Moreover, the Coulombic efficiency of the full cell even reached 99% during cycling, demonstrating highly reversible Na^+ insertion/extraction behaviors. The results suggest large potential application of the free-standing MNTP-TP@rGO nanocomposite in high-performance SIBs.

4 Conclusion

In summary, a free-standing 3D nanocomposite constructed by reduced graphene oxide (rGO), thermally-treated protein (TP) and mesoporous NTP (MNTP) nanocrystals (denoted as MNTP-TP@rGO) is prepared via an electrostatic self-assembly, freeze-drying, mechanical pressing and thermal treatment. In the MNTP-TP@rGO nanocomposite, 3D interconnected carbon network of rGO and TP acts as both a buffer for the anchored well-distributed MNTP nanocrystals and a current collector besides a provider of 3D conduction pathway enabling rapid charge transfer, which benefit the improvement of sodium storage performance. When the free-standing MNTP-TP@rGO nanocomposite is used directly as a anode in coin-type half-cell, it exhibits a high capacity of 114 $mAhg^{-1}$ at 1C, excellent rate capacity of 52 $mAhg^{-1}$ at 50C, and robust cycling stability with the capacity remains of 80% after 1000 cycles at 5C. Furthermore, the fabricated full Na-ion battery using NVP/C as a cathode and free-standing MNTP-TP@rGO nanocomposite as a anode demonstrates a high initial capacity of 58 $mAhg^{-1}$ and 98% capacity retention over 100 cycles at 1C. The free-standing MNTP-TP@rGO nanocomposite has great potential in high-performance SIBs.

Acknowledgements This work was financially supported by the Grants from National Natural Science Foundation of China (Nos. 11474242, 51472209 and 11774298) and the Hunan Provincial Innovation Foundation for Graduate (No. CX2016B254).

References

1. J.-Y. Luo, W.-J. Cui, P. He, Y.-Y. Xia, Raising the cycling stability of aqueous lithium-ion batteries by eliminating oxygen in the electrolyte. Nat. Chem. **2**, 760–765 (2010)
2. X. Wang, X. Lu, B. Liu, D. Chen, Y. Tong, G. Shen, Flexible energy-storage devices: design consideration and recent progress. Adv. Mater. **26** 4763–4782 (2014)
3. X. Xiang, K. Zhang, J. Chen, Recent advances and prospects of cathode materials for sodium-ion batteries. Adv. Mater. **27**, 5343–5364 (2015)
4. C.-X. Zu, H. Li, Thermodynamic analysis on energy densities of batteries. Energy Environ. Sci. **4**, 2614–2624 (2011)
5. C.M. Burba, R. Frech, Vibrational spectroscopic study of lithium intercalation into $LiTi_2(PO_4)_3$. Solid State Ionics **177**, 1489–1494 (2006)
6. W. Shen, C. Wang, Q. Xu, H. Liu, Y. Wang, Nitrogen-doping-induced defects of a carbon coating layer facilitate Na-storage in electrode materials. Adv. Energy Mater. **5**, 1400982 (2015)
7. Y. Wang, L. Zhang, Y. Wu, Y. Zhong, Y. Hu, X.W.D. Lou, Carbon-coated Fe_3O_4 microspheres with a porous multideck-cage structure for highly reversible lithium storage. Chem. Commun. **51**, 6921–6924 (2015)
8. H. Pan, Y.-S. Hu, L. Chen, Room-temperature stationary sodium-ion batteries for large-scale electric energy storage. Energy Environ. Sci. **6**, 2338–2360 (2013)
9. Y. Xu, M. Zhou, X. Wang, C. Wang, L. Liang, F. Grote, M. Wu, Y. Mi, Y. Lei, Enhancement of sodium ion battery performance enabled by oxygen vacancies. Angew. Chem. Int. Ed. **54**, 8768–8771 (2015)
10. N. Yabuuchi, K. Kubota, M. Dahbi, S. Komaba, Research development on sodium-ion batteries. Chem. Rev. **114**, 11636–11682 (2014)
11. J. Chen, G. Zou, H. Hou, Y. Zhang, Z. Huang, X. Ji, Pinecone-like hierarchical anatase TiO_2 bonded with carbon enabling ultrahigh cycling rates for sodium storage. J. Mater. Chem. A **4**, 12591–12601 (2016)
12. G. Xu, L. Yang, X. Wei, J. Ding, J. Zhong, P. Chu, Highly-crystalline ultrathin gadolinium doped and carbon-coated $Li_4Ti_5O_{12}$ nanosheets for enhanced lithium storage. J. Power Sources **295**, 305–313 (2015)
13. X. Xiong, W. Luo, X. Hu, C. Chen, L. Qie, D. Hou, Y. Huang, Flexible membranes of MoS_2/C nanofibers by electrospinning as binder-free anodes for high-performance sodium-ion batteries. Sci. Rep. **5**, 9254 (2015)
14. Y. Cao, L. Xiao, M.L. Sushko, W. Wang, B. Schwenzer, J. Xiao, Z. Nie, L.V. Saraf, Z. Yang, J. Liu, Sodium ion insertion in hollow carbon nanowires for battery applications. Nano Lett. **12**, 3783–3787 (2012)
15. K. Kuratani, M. Yao, H. Senoh, N. Takeichi, T. Sakai, T. Kiyobayashi, Na-ion capacitor using sodium pre-doped hard carbon and activated carbon. Electrochim. Acta **76**, 320–325 (2012)
16. D. Stevens, J. Dahn, High capacity anode materials for rechargeable sodium-ion batteries. J. Electrochem. Soc. **147**, 1271–1273 (2000)
17. Z. Jian, W. Han, X. Lu, H. Yang, Y.-S. Hu, J. Zhou, Z. Zhou, J. Li, W. Chen, D. Chen, Superior electrochemical performance and storage mechanism of $Na_3V_2(PO_4)_3$ cathode for room-Temperature sodium-Ion batteries. Adv. Energy Mater. **3**, 156–160 (2013)

18. Y.H. Jung, C.H. Lim, D.K. Kim, Graphene-supported $Na_3V_2(PO_4)_3$ as a high rate cathode material for sodium-ion batteries. J. Mater. Chem. A **1**, 11350–11354 (2013)
19. X. Wu, Y. Cao, X. Ai, J. Qian, H. Yang, A low-cost and environmentally benign aqueous rechargeable sodium-ion battery based on $NaTi_2(PO_4)_3$–$Na_2NiF(CN)_6$ intercalation chemistry. Electrochem. Commun. 31, 145–148 (2013)
20. Z. Li, D. Young, K. Xiang, W.C. Carter, Y.-M. Chiang, Towards high power high energy aqueous sodium-ion batteries: the $NaTi_2(PO_4)_3/Na_{0.44}MnO_2$ system. Adv. Energy Mater. **3**, 290–294 (2013)
21. Y. Fang, L. Xiao, J. Qian, X. Ai, H. Yang, Y. Cao, Mesoporous amorphous $FePO_4$ nanospheres as high-performance cathode material for sodium-ion batteries. Nano Lett. **14**, 3539–3543 (2014)
22. Y. Fang, L. Xiao, J. Qian, Y. Cao, X. Ai, Y. Huang, H. Yang, 3D graphene decorated $NaTi_2(PO_4)_3$ microspheres as a superior high-rate and ultracycle-stable anode material for sodium ion batteries. Adv. Energy Mater. **6**, 1502197 (2016)
23. S.I. Park, I. Gocheva, S. Okada, J. Yamaki, Electrochemical properties of $NaTi_2(PO_4)_3$ anode for rechargeable aqueous sodium-ion batteries. J. Electrochem. Soc. **158**, A1067–A1070 (2011)
24. C. Chen, Y. Wen, X. Hu, X. Ji, M. Yan, L. Mai, P. Hu, B. Shan, Y. Huang, Na+ intercalation pseudocapacitance in graphene-coupled titanium oxide enabling ultra-fast sodium storage and long-term cycling. Nat. Commun. **6**, 7929 (2015)
25. G. Pang, C. Yuan, P. Nie, B. Ding, J. Zhu, X. Zhang, Synthesis of NASICON-type structured $NaTi_2(PO_4)_3$–graphene nanocomposite as an anode for aqueous rechargeable Na-ion batteries. Nanoscale **6**, 6328–6334 (2014)
26. B. Qu, C. Ma, G. Ji, C. Xu, J. Xu, Y.S. Meng, T. Wang, J.Y. Lee, Layered SnS_2-reduced graphene oxide composite–a high-capacity, high-rate, and long-cycle life sodium-ion battery anode material. Adv. Mater. **26**, 3854–3859 (2014)
27. D. Su, S. Dou, G. Wang, WS_2@ graphene nanocomposites as anode materials for Na-ion batteries with enhanced electrochemical performances. Chem. Commun. **50**, 4192–4195 (2014)
28. G. Xu, L. Yang, X. Wei, J. Ding, J. Zhong, P. Chu, Hierarchical porous nanocomposite architectures from multi-wall carbon nanotube threaded mesoporous $NaTi_2(PO_4)_3$ nanocrystals for high-performance sodium electrodes. J. Power Sources **327**, 580–590 (2016)
29. Q. An, F. Xiong, Q. Wei, J. Sheng, L. He, D. Ma, Y. Yao, L. Mai, Nanoflake-Assembled Hierarchical $Na_3V_2(PO_4)_3$/C microflowers: superior li storage performance and insertion/extraction mechanism. Adv. Energy Mater. **5**, 1401963 (2015)
30. G. Xu, L. Yang, Z. Li, X. Wei, P.K. Chu, Protein-assisted assembly of mesoporous nanocrystals and carbon nanotubes for self-supporting high-performance sodium electrodes. J. Mater. Chem. A **5**, 2749–2758 (2017)
31. W. Wu, A. Mohamed, J. Whitacre, Microwave synthesized $NaTi_2(PO_4)_3$ as an aqueous sodium-ion negative electrode. J. Electrochem. Soc. **160**, A497–A504 (2013)
32. H.-K. Roh, H.-K. Kim, M.-S. Kim, D.-H. Kim, K.Y. Chung, K.C. Roh, K.-B. Kim, In situ synthesis of chemically bonded $NaTi_2(PO_4)_3$/rGO 2D nanocomposite for high-rate sodium-ion batteries. Nano Res. **9**, 1844–1855 (2016)
33. G. Pang, P. Nie, C. Yuan, L. Shen, X. Zhang, H. Li, C. Zhang, Mesoporous $NaTi_2(PO_4)_3$/CMK-3 nanohybrid as anode for long-life Na-ion batteries. J. Mater. Chem. A **2**, 20659–20666 (2014)
34. G. Yang, H. Song, M. Wu, C. Wang, Porous $NaTi_2(PO_4)_3$ nanocubes: a high-rate nonaqueous sodium anode material with more than 10000 cycle life. J. Mater. Chem. A **3**, 18718–18726 (2015)
35. C. Wu, P. Kopold, Y.-L. Ding, P.A. van Aken, J. Maier, Y. Yu, Synthesizing porous $NaTi_2(PO_4)_3$ nanoparticles embedded in 3D graphene networks for high-rate and long cycle-life sodium electrodes. ACS Nano **9**, 6610–6618 (2015)